

POLO: Localizing RFID-Tagged Objects for Mobile Robots

Dianhan Xie, Xudong Wang, Aimin Tang, and Hongzi Zhu
Shanghai Jiao Tong University, Shanghai, China

Email: {dianhanxie, wxudong, tangaiming}@sjtu.edu.cn, hongzi@cs.sjtu.edu.cn

Abstract—In many Internet-of-Things (IoT) applications, various RFID-tagged objects need to be localized by mobile robots. Existing RFID localization systems are infeasible, since they either demand bulky RFID infrastructures or cannot achieve sufficient localization accuracy. In this paper, a portable localization (POLO) system is developed for a mobile robot to locate RFID-tagged objects. Besides a single RFID reader on board, POLO is distinguished with a tag array and a lightweight receiver. The tag array is designed to reflect the RFID signal from an object into multi-path signals. The receiver captures such signals and estimates their multi-path channel coefficients by a tag-array-assisted channel estimation (TCE) mechanism. Such channel coefficients are further exploited to determine the object’s direction by a spatial smoothing direction estimation (SSDE) algorithm. Based on the object’s direction, POLO guides the robot to approach the object. When the object is in proximity, its 2D location is finally determined by a near-range positioning (NRP) algorithm. POLO is prototyped and evaluated via extensive experiments. Results show that the average angular error is within 1.6 degrees when the object is in the far-range (2~6 m), and the average location error is within 5 cm while the object is in the near-range (~1 m).

I. INTRODUCTION

Many new Internet-of-Things (IoT) applications require to accurately locate RFID-tagged objects on mobile robots. For example, in smart manufacturing, robots need to locate the products or the components in assembly lines, or in unmanned express delivery, robots need to locate and sort packages. A portable localization system is required in such applications.

In the literature, there are two categories of systems for locating RFID-tagged objects. In the first category [1]–[4], multiple RFID reader antennas are deployed in a well-designed way to implement an antenna array. The phases of the channel coefficients between the object and the antenna array are exploited to determine the object’s location. However, to achieve sufficient localization accuracy (10~20 cm), at least four RFID reader antennas are required in these schemes. As each RFID reader antenna is typically in size of $26\text{cm} \times 26\text{cm} \times 4\text{cm}$, the first category is infeasible for mobile robots. In the second category [5]–[7], an RFID reader antenna is carried by a moving equipment, and a high-accuracy localization system is deployed to track the real-time location of the antenna (sub-cm accuracy). An antenna array is then emulated by synthetic aperture radar (SAR) technology [8]. However, the high-accuracy tracking of moving RFID antennas restricts the mobility of the moving equipment, by requiring its movement on a linear guide [5] or a rail [7],

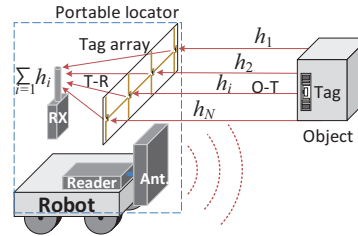


Fig. 1. POLO system.

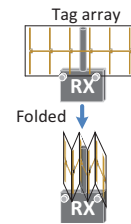


Fig. 2. Tag array and RX.

or demanding support from an anchor [6]. Such restrictions make these schemes infeasible for mobile robots due to their roaming in the entire factory.

In this paper, a portable localization system, called POLO, is developed for mobile robots to locate RFID-tagged objects. As shown in Figure 1, POLO consists of a portable locator designed in this paper. The locator consists of a single RFID reader, a tag array and a lightweight receiver. The reader is used for interrogating the RFID tag on an object. The tag array reflects the signals from the object into multi-path signals by multiple tag elements. The receiver captures such signals and estimates the channel coefficient of the path reflected by each tag element (i.e., $h_i, i = 1, 2, \dots$, in Figure 1). The tag array can be folded up to a small size as shown in Figure 2, so that it is convenient to be carried. Based on the channel coefficients ($h_i, i = 1, 2, \dots$), a two-step localization approach is developed. In the first step, the object’s direction is determined to guide the robot to approach the object. In the second step, when the object is detected to be in proximity, its 2D location is determined.

There are three main challenges in POLO design. First, the signals reflected by the tag elements are superimposed together at the receiver. Only the combined channel coefficient ($\sum_i h_i$) can be estimated. To tackle this challenge, a tag-array-assisted channel estimation (TCE) mechanism is designed. In TCE, the reflection coefficient of each tag element is changed by switching on or off each element sequentially. The channel coefficients ($h_i, i = 1, 2, \dots$) are then estimated by the channel variations induced by the tag element switching.

Second, the path from each tag element to the receiver (denoted as **T-R path**) induces an offset in the channel coefficient (h_i), and thus affects the ultimate localization results. To this end, a channel coefficient calibration (CCC) mechanism is designed to eliminate the impact of the T-R

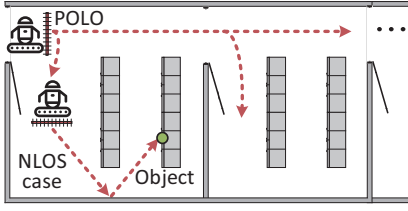


Fig. 3. Application scenarios.

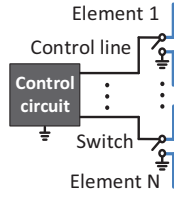


Fig. 4. Tag array circuit.

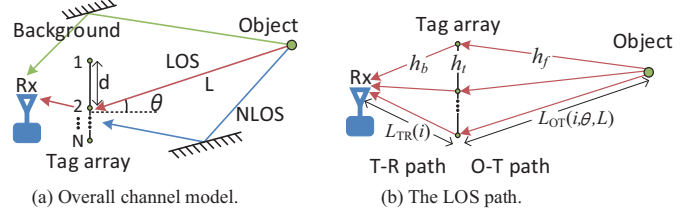


Fig. 5. The channel model in POLO.

path.

Third, the channel coefficient (h_i) is affected by the mutual coupling between the tag elements of the tag array. Particularly, the mutual coupling varies with the incidence direction of radio signals, which is referred to as **anisotropic coupling** in this paper. Thus, the existing solution to resisting multipath reflections from environment, i.e., the spatial smoothing algorithm [9], [10], becomes ineffective for the following reason. The impacts of anisotropic coupling on different tag elements are different. Although the tag elements are equally spaced, the tag array cannot be regarded as a uniform linear array, and thus the spatial smoothing algorithm cannot be applied. To tackle this challenge, a coupling impact modeling (CIM) mechanism is designed to model the impact of the anisotropic coupling. Based on this model, anisotropic coupling is eliminated in the two-step localization approach. In the far range, anisotropic coupling is eliminated by obtaining an equivalent uniform array. Based on the equivalent uniform array, a spatial smoothing direction estimation (SSDE) algorithm is designed to estimate the object's direction. In the near range, a near-range positioning (NRP) algorithm is designed to eliminate anisotropic coupling and estimate the object's 2D location.

POLO is implemented via a prototyping system that consists of an 11-tag array, a USRP N210 device, and a commercial-off-the-shelf (COTS) RFID reader. Extensive experiments are conducted in various indoor scenarios (room and corridor) and use cases (mobile and static). The experimental results demonstrate that the average angular error is within 1.6° in the far range ($2 \sim 6$ m), and the average location error is within 5 cm in the near range (~ 1 m).

POLO has four advantages over the existing RFID localization systems. First, POLO is not restricted to a fixed place. The robot with POLO can move around to locate RFID-tagged objects in a large scale area, as shown in Figure 3. Second, POLO can locate an object in non-line-of-sight (NLOS) case (LOS path is absent), as shown by the NLOS case in Figure 3. POLO measures the direction of a reflection path from the object, and guides the robot to approach the object via the reflection path. Third, POLO improves the navigation capability of a robot. Fourth, POLO is lightweight, low-cost, and easy to deploy. The contributions of this paper are highlighted as follows.

- To the best of our knowledge, POLO is the first portable localization system for mobile robots to locate the RFID-tagged objects.

- The main challenges in POLO design are solved by a series of novel mechanisms, including TCE, CCC, CIM, and a two-step localization approach.
- POLO is evaluated via a prototyping implementation.

The rest of this paper is organized as follows. The system model and channel model are presented in Section II. The design of POLO is elaborated in Section III. The prototype implementation and evaluation are carried out in Section IV and Section V, respectively. The related work is presented in Section VI. The paper is concluded in Section VII.

II. SYSTEM MODEL AND CHANNEL MODEL

A. System Model

There are two entities in POLO system.

The first entity is an RFID-tagged object. It is distinguished by an RFID tag on it. If the RFID tag is queried by an RFID reader, it will reply its ID information.

The second entity is a portable locator. It is deployed on the mobile robot to locate the RFID-tagged objects. It consists of a COTS RFID reader, a tag array, and a radio receiver. The reader is used to interrogate the RFID tag on the object. The tag array consists of multiple equally spaced tag elements. The reflection coefficient of each tag element are controlled by a circuit via an electronic switch [11], as shown in Figure 4. The support of the tag array is attached to the receiver. The receiver has a pigtail antenna and can acquire the RFID signals for localization.

B. Channel Model

The channel model between the receiver and the object in POLO is presented as follows. The overall channel model is shown in Figure 5(a). There are three categories of channel paths in this system: 1) **Background path**: the path along which the signal is reflected by surroundings (except the tag array) and received by the receiver; 2) **LOS path**: the path along which the signal arrives at the tag array through LOS and finally reaches the receiver; 3) **NLOS path**: the path along which the signal is reflected by surroundings, reflected again by the tag array, and received by the receiver.

1) *The channel model in the LOS path*: The tag array consists of N tag elements that are uniformly placed in a straight line, as shown in Figure 5(a). The element spacing is d . The distance between the center point of the tag array and the object is L . The direction of the object is θ , which is defined by the angle between the line from the middle point of the tag array to the object and the perpendicular direction

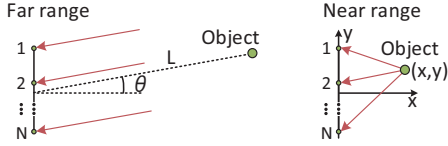


Fig. 6. Far range and near range.

of the tag array. Thus, the object's location is characterized by L and θ .

The channel model in the LOS path is shown in Figure 5(b). The channel coefficient of the LOS path from tag element i is denoted by h_i^{los} , which is determined by three factors:

- The channel coefficient of the path from the object to the i -th tag element (called the i -th **O-T** path):

$$h_f(i, \theta, L) = |h_f(i, \theta, L)| e^{\frac{j2\pi L_{OT}(i, \theta, L)}{\lambda}}, \quad (1)$$

where λ is the carrier wavelength, and $L_{OT}(i, \theta, L)$ is the length of i -th O-T path.

- The channel coefficient induced by the tag array: $h_t(i, \theta, L)$. Based on the observational experiments in Section III-D, $h_t(i, \theta, L)$ varies with θ and L , which is referred to as **anisotropic coupling**.
- The channel coefficient of the path from the i -th tag element to the receiver (called the i -th **T-R** path): $h_b(i) = |h_b(i)| e^{\frac{j2\pi L_{TR}(i)}{\lambda}}$, where $L_{TR}(i)$ is the length of the i -th T-R path, which is fixed in this system.

Thus, h_i^{los} is expressed as

$$h_i^{los} = h_f(i, \theta, L) h_t(i, \theta, L) h_b(i). \quad (2)$$

Based on Eqs. (1) and (2), it can be observed that the location information (L and θ) is in the phase component of $h_f(i, \theta, L)$, i.e., $L_{OT}(i, \theta, L)$. If $h_t(i, \theta, L)$ and $h_b(i)$ are removed, $h_f(i, \theta, L)$ can be obtained, and the object's location can be determined.

Nevertheless, the phase of $h_f(i, \theta, L)$ is a periodic function with period λ , as $\text{mod}(\frac{2\pi L_{OT}(i, \theta, L)}{\lambda}, 2\pi)$, which leads to ambiguity in localization based on phase. To address this issue, the tag element spacing (d) is set within $\lambda/2$, and thus the difference between $L_{OT}(i, \theta, L)$ of any two adjacent elements is in $[-\lambda/2, \lambda/2]$. In this way, the object tag can be located by the phase differences among $h_f(i, \theta, L)$.

2) *Channel model of NLOS paths*: Suppose there are M NLOS paths, the channel coefficient of the NLOS paths (denoted by h_i^{nlos}) is expressed as,

$$h_i^{nlos} = \sum_{m=1}^M h_f(i, \theta_m, L_m) h_t(i, \theta_m, L_m) h_b(i), \quad (3)$$

where θ_m and L_m is the direction and the length of the m -th NLOS path through the i -th tag element, respectively.

The signals from the LOS path and the NLOS paths are superimposed at the tag array. The combined channel coefficient of the paths reflected by the i -th tag element (denoted by h_i) is expressed as

$$h_i = h_i^{los} + h_i^{nlos}. \quad (4)$$

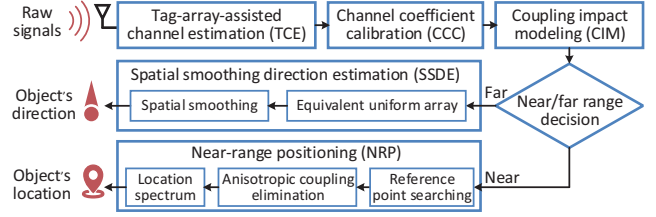


Fig. 7. The function blocks in POLO.

3) *The overall channel model*: As the receiver has a single antenna, the signals reflected by the tag array and that from the background paths are superimposed together. The channel coefficient between the object and the receiver at time t is,

$$h(t) = \sum_{i=1}^N h_i + h_o(t), \quad (5)$$

where $h_o(t)$ is the combined channel coefficient of all the background paths.

4) *Far range and near range*: An important property should be noted: When the object is far from the tag array, the O-T paths are almost parallel with each other, as shown by the far range case in Figure 6. The phase differences among $h_f(i, \theta, L)$ are not sensitive to the object's distance L . Only the object's direction can be determined. When the object is in the proximity of the tag array, the phase differences among $h_f(i, \theta, L)$ is sensitive to both the object's distance L and the object's direction θ , as shown by the near range case in Figure 6. The object's 2D location can be determined.¹

To locate the object, a) the channel coefficients in the tag array ($h_t(i, \theta, L)$) and the T-R path ($h_b(i)$) need to be eliminated; b) the interference from the background paths ($h_o(t)$) and the NLOS paths (h_i^{nlos}) need to be resisted.

III. DESIGN OF POLO

A. Overview

In POLO, the backscattered RFID signal from the object is further reflected by the tag array into multi-path signals, and acquired by the receiver in the portable locator. The channel coefficients of such multi-path signals are estimated and calibrated for locating the object. When the object is in the far range (2~6 m), the object's direction can be determined. When the object is in the near range (~1 m), POLO can recognize the near range case, and determine the object's 2D location. POLO is designed with six key function blocks, as shown in Figure 7:

- **Tag-array-assisted channel estimation (TCE)**: TCE is designed to estimate the channel coefficients h_i , and to remove the interference from the background paths.
- **Channel coefficient calibration (CCC)**: CCC is designed to eliminate the impact of T-R path.

¹For the ease of presentation, in the near range, the location of the object is expressed by a Cartesian coordinate system (x, y) , where $x = L \cos(\theta)$ and $y = L \sin \theta$, as shown in Figure 6.

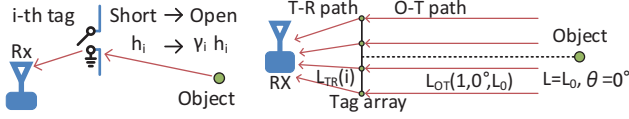


Fig. 8. Tag element switching. Fig. 9. Channel coefficient calibration.

- **Coupling impact modeling (CIM):** CIM is designed to model the impact of anisotropic coupling. Both the far-range model and the near-range model can be obtained.
- **Spatial smoothing direction estimation (SSDE):** In the far range, SSDE is developed to eliminate anisotropic coupling via an equivalent uniform array, and to determine the object's direction via a spatial smoothing algorithm.
- **Near-range positioning (NRP):** In the near range, NRP is designed to eliminate anisotropic coupling based on the coupling impact model, and to determine the object's 2D location via a location spectrum.
- **Near/far range decision:** The near/far range decision is designed to determine whether the object is in proximity.

B. Tag-Array-Assisted Channel Estimation

TCE is designed to estimate the channel coefficients h_i . Since the receiver only has a single antenna, the signals reflected by the tag elements are superimposed together at the receiver. The conventional channel estimation schemes [12] can only estimate the combined channel coefficient between the object and the receiver, which is expressed by

$$\hat{h}(t) = \sum_{i=1}^N h_i + h_o(t) + w_h(t), \quad (6)$$

where $\hat{h}(t)$ is the estimated channel coefficient at time t , and $w_h(t)$ is the noise in channel estimation procedure.

To obtain the channel coefficients of the N paths from the tag array, TCE is conducted in $N+1$ time slots. In the first slot $t = t_0$, the electronic switches of all tag elements are shorted. In the slot $t = t_i$, only the electronic switch of the i -th tag element is open, as shown in Figure 8. As a result, the channel coefficient of i -th path is changed from h_i to $\gamma_i h_i$, where γ_i is a complex constant determined by the characteristic of the i -th tag element. In each slot, the combined channel coefficient between the object and the receiver, i.e., $\hat{h}(t)$ is estimated. This procedure proceeds until all tag elements have been opened once.

The estimated channel coefficient of the i -th path (denoted by \hat{h}_i) is acquired by the difference between the combined channel coefficients at t_0 and t_i , i.e., $\hat{h}(t_0)$ and $\hat{h}(t_i)$, as

$$\begin{aligned} \hat{h}_i &= \hat{h}(t_i) - \hat{h}(t_0) \\ &= (\gamma_i - 1)h_i - [h_o(t_i) - h_o(t_0)] - [w_h(t_i) - w_h(t_0)]. \end{aligned} \quad (7)$$

where $(\gamma_i - 1)$ is a constant whose impact to h_i can be eliminated by the CCC mechanism in Section III-C. The noise term $[w_h(t_i) - w_h(t_0)]$ can be suppressed by increasing the number of received samples in the channel estimation procedure. However, $h_o(t_i) - h_o(t_0)$ is the channel variation

of the background paths from t_0 to t_i , which is not negligible, especially in a dynamic environment.

To resist the channel variation of the background paths ($h_o(t_i) - h_o(t_0)$), the time slot duration of each state is set to 0.05 millisecond. In such a short interval, the channel variation of the background paths is negligible. Besides, TCE proceeds repeatedly to acquire sufficient samples to suppress the noise term in Eq. (7). Thus, the channel coefficients of the paths through the tag array h_i can be estimated as

$$\hat{h}_i \approx (\gamma_i - 1)h_i. \quad (8)$$

C. Channel Coefficient Calibration

CCC is designed to eliminate both the channel coefficient in the T-R path ($h_b(i)$ in Eq. (2)) and the parameter induced by TCE ($\gamma_i - 1$ in Eq. (8)). As the support of the tag array is attached to the receiver, the above parameters are constant numbers. Hence, CCC is only conducted once during system initialization.

In CCC, the first step is to measure the channel coefficient in the T-R path. There are two requirements in this measurement:

Requirement 1: To avoid the influence of the NLOS paths, the measurement is conducted in an open space, e.g., outdoors.

Requirement 2: To avoid the impact of the O-T paths, an object RFID tag is placed at the perpendicular direction of the tag array ($\theta = 0^\circ$), and in the far range ($L = L_0$), as shown in Figure 9. Thus, the channel coefficients of the O-T paths are equal, i.e., $h_f(i, 0^\circ, L_0) = h_f(1, 0^\circ, L_0)$, $i = 1, \dots, N$.

The measured channel coefficient h_i is recorded for calibration, and denoted by \hat{h}_i^0 . Based on the Eqs. (2), (4), and (8), \hat{h}_i^0 is expressed as

$$\hat{h}_i^0 = (\gamma_i - 1)h_f(1, 0^\circ, L_0)h_t(i, 0^\circ, L_0)h_b(i), i \in [1, N]. \quad (9)$$

In the second step, the estimated channel coefficients \hat{h}_i in TCE are calibrated as $h_i^c = \hat{h}_i \cdot (\hat{h}_i^0)^{-1}$, where h_i^c is the calibrated channel coefficient after performing CCC. Based on Eqs. (2), (3), (4), (8) and (9), h_i^c can be expressed as

$$h_i^c = \frac{h_f(i, \theta, L)h_t(i, \theta, L) + \sum_{m=1}^M h_f(i, \theta_m, L_m)h_t(i, \theta_m, L_m)}{h_f(1, 0^\circ, L_0)h_t(i, 0^\circ, L_0)}. \quad (10)$$

Hence, $h_b(i)$ and $(\gamma_i - 1)$ are eliminated.

D. Coupling Impact Modeling

1) **Anisotropic coupling:** The anisotropic coupling affects the calibrated channel coefficient h_i^c . The reason of anisotropic coupling is that the radiation patterns of the tag elements on the tag array are coupled with each other [13]. The coupling pattern varies with the incidence direction of the radio signals at tag elements. Particularly, the incidence direction of the radio signals at each tag element is determined by the object's 2D location in the near range (as the O-T paths are not parallel with each other), and is determined by the object's direction in the far range.

Hence, anisotropic coupling is revealed via two sets of observational experiments. They are conducted outdoors to

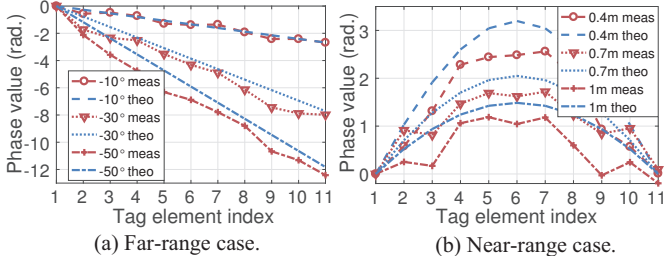


Fig. 10. Influence of anisotropic coupling in a 11-tag array. The measured results and the theoretical results are represented by ‘meas’ and ‘theo’, respectively.

remove other influence factors such as multipath reflections. The first set of experiments are conducted in the far range where an object is placed at different directions (-10° , -30° and -50°). The second set of experiments are conducted in the near range where an object is placed at different locations ($(0.4m, 0m)$, $(0.7m, 0m)$, and $(1m, 0m)$). The phase values of the calibrated channel coefficients (h_i^c) in the first set and the second set of experiments are shown in Figures. 10(a) and 10(b), respectively. To reveal the impact of anisotropic coupling, the theoretical phase values of the channel coefficients are derived based on the object’s true locations, as $\frac{2\pi L_{OT}(i, \theta, L)}{\lambda}$. The theoretical results are shown by the dashed lines in Figures. 10(a) and 10(b). Two observations are as follows:

Observation 1: The measured phase values deviate from the theoretical values. The deviations are different for different tag elements. Moreover, the deviation can exceed one radian, which greatly degrades localization.

Observation 2: The phase differences between the measured channel coefficients and the theoretical values vary with the object’s location (i.e., direction in the far range and 2D location in the near range).

2) *Process of CIM:* CIM is to characterize the impact of anisotropic coupling on the calibrated channel coefficient h_i^c . The model consists of a set of calibrated channel coefficients corresponding to different directions in the far range, or a set of calibrated channel coefficients corresponding to different locations in the near range. They are used to eliminate anisotropic coupling in SSDE scheme and NRP scheme, respectively.

The measurement is conducted in an open space to avoid the impact of multipath reflections, and is conducted in both the far range and the near range. In the far range, the direction of the tag varies from -75° to 75° with a step of 1° , as shown in Figure 11(a). At each direction, the channel coefficient of the path reflected by each tag element is estimated by TCE, and calibrated by CCC. The calibrated channel coefficient h_i^c is collected as the coupling impact model in the far range. These coefficients are denoted as $h_{cm}^\alpha(i, \theta_l)$, where $\theta_l \in [-75^\circ, 75^\circ]$.

In the near range, the tag is placed at 21×21 reference points individually in a $1m \times 1m$ rectangular area, as shown in Figure 11(b). The distance between two adjacent calibration points is 5 cm. The tag array is placed at the left border of

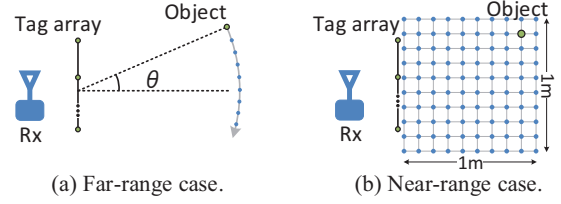


Fig. 11. Coupling impact modeling.

the rectangular area. At each reference point, the calibrated channel coefficient h_i^c is collected as the coupling impact model in the near range. These channel coefficients are denoted as $h_{cm}^\beta(i, x_l, y_l)$, where $x_l \in [0cm, 100cm]$ and $y_l \in [-50cm, 50cm]$.

It should be mentioned that CIM can be conducted in a one-time initialization procedure, as anisotropic coupling of a certain tag array is time-invariant and is independent from environment. Hence, CCC and CIM can be conducted once forever, which does not add extra workload for users.

E. Spatial Smoothing Direction Estimation (SSDE)

When an object is in the far range, the O-T paths can be regarded as parallel with each other, as shown in Figure 12. The relation between the channel coefficient of the O-T path $h_f(i, \theta, L)$ and the object’s direction θ in Eq. (1) is expressed as

$$h_f(i, \theta, L) \approx h_f(1, \theta, L) e^{\frac{j2\pi(i-1)d \sin \theta}{\lambda}}, \quad (11)$$

where $|h_f(i, \theta, L)| \approx |h_f(1, \theta, L)|$, as the distances between the tag elements are far smaller than the distance between the tag array and the object. In Eq. (11), the phase differences between any two adjacent elements of $h_f(i, \theta, L)$ are identical, i.e., $\frac{2\pi d \sin \theta}{\lambda}$, which is a crucial property of uniform linear arrays. It seems that the spatial smoothing algorithm in [9], [10] can be applied to estimate the object’s direction and resist the interference from NLOS paths. However, $h_f(i, \theta, L)$ cannot be obtained in our system, and the tag array cannot be regarded as a uniform linear array. The reason is that the impacts of anisotropic coupling on different tag elements are different, which destroys the property of a uniform linear array.

1) *Equivalent uniform array:* To combat the anisotropic coupling, an equivalent uniform array is designed based on the coupling impact model $h_{cm}^\alpha(i, \theta)$. The equivalent uniform array is an ideal uniform linear array without impact of mutual coupling, and is equivalent to the true tag array in all directions. Based on such an equivalent uniform array, the spatial smoothing algorithm can be applied.

The channel model of the equivalent uniform array is denoted by a vector $\mathbf{a}_v(\theta)$ as,

$$\mathbf{a}_v(\theta) = \left[1, e^{\frac{j2\pi d_v(\theta) \sin \theta}{\lambda}}, \dots, e^{\frac{j2\pi(N-1)d_v(\theta) \sin \theta}{\lambda}} \right]^T, \quad (12)$$

where $d_v(\theta)$ is the element spacing of the equivalent uniform array (and thus it is *equivalent element spacing*).

At each direction θ , $d_v(\theta)$ is obtained by ensuring $\mathbf{a}_v(\theta)$ and the normalized coupling impact model, i.e.,

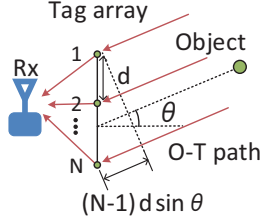


Fig. 12. Channel model in the far range.

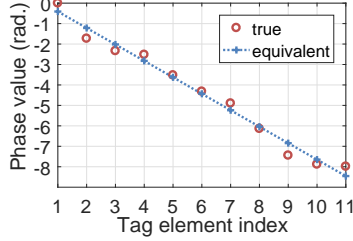


Fig. 13. Equivalent model in -30° direction.

$[e^{j\phi_{cm}^\alpha(1,\theta)}, \dots, e^{j\phi_{cm}^\alpha(N,\theta)}]$, as close as possible, where $\phi_{cm}^\alpha(i, \theta)$ is the phase of $h_{cm}^\alpha(i, \theta)$. Hence,

$$d_v(\theta) = \arg \max_d \left| \sum_{i=1}^N e^{j\left[\frac{2\pi(i-1)d \sin \theta}{\lambda} - \phi_{cm}^\alpha(i, \theta)\right]} \right|. \quad (13)$$

The calibrated channel coefficients $[h_1^c, \dots, h_N^c]^\top$ in Eq. (10) can be expressed in form of $\mathbf{a}_v(\theta)$. If there is only the LOS path between the tag array and the object ($M = 0$),

$$\begin{bmatrix} h_1^c \\ \vdots \\ h_N^c \end{bmatrix} = \frac{h_f(1, \theta, L)}{h_f(1, 0^\circ, L_0)} \mathbf{a}_v(\theta) + \begin{bmatrix} w_{1,0} \\ \vdots \\ w_{N,0} \end{bmatrix}, \quad (14)$$

where $w_{i,0}$ is the approximation error between the equivalent model and the true model. An example of the equivalent uniform array and the true array in -30° direction is shown in Figure 13.

Considering that there are M NLOS paths, the channel coefficients $[h_1^c \dots h_N^c]^\top$ are expressed as

$$\begin{bmatrix} h_1^c \\ \vdots \\ h_N^c \end{bmatrix} = \frac{[\mathbf{a}_v(\theta) \dots \mathbf{a}_v(\theta_M)]}{h_f(1, 0^\circ, L_0)} \begin{bmatrix} h_f(1, \theta, L) \\ h_f(1, \theta_1, L_1) \\ \vdots \\ h_f(1, \theta_M, L_M) \end{bmatrix} + \sum_{m=0}^M \begin{bmatrix} w_{1,m} \\ \vdots \\ w_{N,m} \end{bmatrix}. \quad (15)$$

2) *Spatial smoothing*: Based on the equivalent model in Eq. (15), the spatial smoothing scheme developed in [9], [10] can be applied. The detailed procedure is as follows.

First, the channel coefficients $[h_1^c \dots h_N^c]^\top$ are divided into K subarrays, as shown in Figure 14. In the k -th subarray, the channel coefficient is $[h_k^c \ h_{k+1}^c \dots h_{N-K+k}^c]$, and its correlation matrix is

$$R_{hh,k} = [h_k^c \dots h_{N-K+k}^c]^H [h_k^c \dots h_{N-K+k}^c]. \quad (16)$$

Second, $R_{hh,k}$ is averaged over $k \in \{1, \dots, K\}$ with the average of $\bar{R}_{hh} = \frac{1}{K} \sum_{k=1}^K R_{hh,k}$. \bar{R}_{hh} is required to have full rank, and thus $K \geq \frac{N+1}{2}$. It has $N - K + 1$ eigenvalues $[\sigma_1 \dots \sigma_{M+1} \ \sigma_{M+2} \dots \sigma_{N-K+1}]$ in a decreasing order. The biggest $M + 1$ eigenvalues are corresponding to the LOS path and the M NLOS paths. The next $N - K - M$ eigenvalues are corresponding to the noise term $w_{i,m}$ in Eq. (15). The $N - K + 1$ corresponding eigenvectors are

$$\mathbf{E} = [\mathbf{e}_1 \dots \mathbf{e}_{M+1} \dots \mathbf{e}_{M+2} \dots \mathbf{e}_{N-K+1}], \quad (17)$$

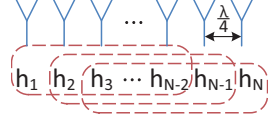


Fig. 14. Spatial smoothing.

where $[\mathbf{e}_1 \dots \mathbf{e}_{M+1}]$ is the *signal subspace*, and denoted as \mathbf{E}_S . $[\mathbf{e}_{M+2} \dots \mathbf{e}_{N-K+1}]$ is the *noise subspace*, and denoted as \mathbf{E}_N .

Third, the MUSIC AoA spectrum in [14] is applied to estimate the directions of the LOS path and NLOS paths as

$$P_D(\theta_s) = [\mathbf{a}_s(\theta_s) \mathbf{E}_N \mathbf{E}_N^* \mathbf{a}_s(\theta_s)^*]^{-1}, \quad (18)$$

where $\mathbf{a}_s(\theta_s) = [1, \dots, \exp(j\frac{2\pi(N-K)d_v(\theta_s) \sin \theta_s}{\lambda})]$. When $\theta_s = \theta, \theta_1, \dots, \theta_M$, $\mathbf{a}_s(\theta_s) \perp \mathbf{E}_N$, and sharp peaks appear in $P_D(\theta_s)$.

3) *LOS/NLOS path recognition*: Based on the MUSIC AoA spectrum, multiple direction values are obtained (including the LOS path and NLOS paths). The direction of the LOS path needs to be recognized. This issue is solved based on a property: the direction of the LOS path is more stable than the directions of NLOS paths, when POLO is moved with the robot through a small distance. This property has been revealed in [10], where the LOS path and NLOS paths can be recognized with an accuracy of 90%. Moreover, an advantage of POLO should be highlighted here. Even if a NLOS path may be recognized as the LOS path (due to stronger signals in a NLOS path), the robot with POLO can still follow the NLOS path to approach the object.

F. Near-Range Positioning

When an object is in the near range (the O-T paths are not parallel), the tag array cannot be regarded as a uniform array even if anisotropic coupling can be eliminated. Hence, SSDE cannot be applied in the near range. A new algorithm NRP is designed to estimate the object's 2D location. First, based on the coupling impact model for the near range, the nearest reference point to the object is determined. As the reference points are densely spaced, the object's possible region is controlled to be within $5\text{cm} \times 5\text{cm}$. To accurately determine the object's location, the phase offset induced by anisotropic coupling is eliminated, and the object's location is finally determined.

1) *Reference point searching*: Given a reference point (x_l, y_l) , if it is close to the object's actual location, the phase of $h_{cm}^\beta(x_l, y_l)$ (denoted by $\phi_{cm}^\beta(i, x_l, y_l)$) is also close to the phases of calibrated channel coefficients h_i^c (denoted by ϕ_i^c). Based on this principle, a location similarity parameter $\Gamma(x_l, y_l)$ is designed to measure the similarity between $\phi_{cm}^\beta(i, x_l, y_l)$ and ϕ_i^c as

$$\Gamma(x_l, y_l) = \frac{1}{N} \left| \sum_{i=1}^N e^{j[\phi_i^c - \phi_{cm}^\beta(i, x_l, y_l)]} \right|. \quad (19)$$

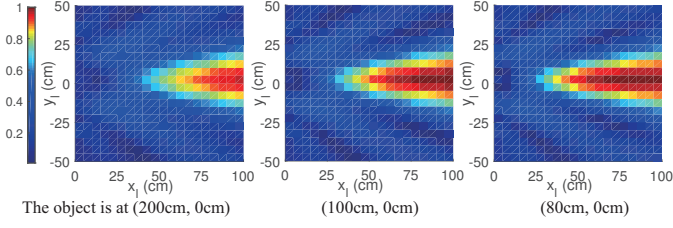


Fig. 15. Similarity map $\Gamma(x_l, y_l)$.

$\Gamma(x_l, y_l)$ reaches the maximum at the nearest reference point (\hat{x}_l, \hat{y}_l) . Hence,

$$(\hat{x}_l, \hat{y}_l) = \arg \max_{(x_l, y_l)} \Gamma(x_l, y_l). \quad (20)$$

2) *Anisotropic coupling elimination*: Based on the reference point (\hat{x}_l, \hat{y}_l) , the phase offset induced by the anisotropic coupling is obtained by the difference between the ideal channel phase (i.e., $\frac{2\pi L_{OT}(i, \hat{x}_l, \hat{y}_l)}{\lambda}$) and the phase in coupling impact model as,

$$\phi_i^\delta = \left[\phi_{cm}^\beta(i, \hat{x}_l, \hat{y}_l) - \frac{2\pi L_{OT}(i, \hat{x}_l, \hat{y}_l)}{\lambda} \right]. \quad (21)$$

The impact of anisotropic coupling is eliminated by $\phi_i^c - \phi_i^\delta$.

3) *Location spectrum*: The object's location (denoted by (\hat{x}, \hat{y})) is determined by calculating a location spectrum as

$$P_L(x, y) = \frac{1}{N} \left| \sum_{i=1}^N e^{j \left[\phi_i^c - \phi_i^\delta - \frac{2\pi L_{OT}(i, x, y)}{\lambda} \right]} \right|. \quad (22)$$

If $(x, y) = (\hat{x}, \hat{y})$, $\phi_i^c - \phi_i^\delta - \frac{2\pi L_{OT}(i, x, y)}{\lambda} = 0$, and then $P_L(x, y)$ reaches the maximum. Hence, the location of the object is determined by

$$(\hat{x}, \hat{y}) = \arg \max_{(x, y)} P_L(x, y). \quad (23)$$

Since NRP is not effective in resisting multipath reflections, it is not applicable to the far range.

G. Near/Far Range Decision

POLO needs to determine if the object is in the near range so that NRP can be applied. This can be achieved via $\Gamma(x_l, y_l)$ as follows. By calculating $\Gamma(x_l, y_l)$ of all reference points, a location similarity map can be built for a certain location of the object. On this map, each point (x_l, y_l) has an associated value of $\Gamma(x_l, y_l)$, as shown in Fig. 15. If the object is closer to the near range, the number of points whose value exceed a threshold (e.g., 0.95) increases. As shown in Fig. 15, when the object is at location (200cm, 0cm), there is only one such point. However, the number of such points increases to 18 points when the object is at (80cm, 0cm). Thus, the number of such points can be used to indicate if the object is in the near range.

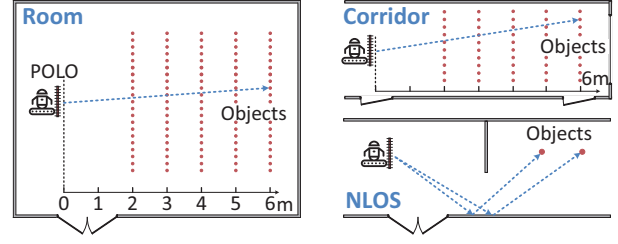


Fig. 16. Experiment setup.

IV. PROTOTYPE IMPLEMENTATION

A. Hardware

1) *Tag array*: A fixed array of eleven tags and a control circuit are implemented. Each element has a dipole antenna, separated at a distance of 8cm, installed via two 7cm copper wires. The reflection coefficient of each tag element is controlled by the control circuit, using an MSP 430 microcontroller [15] and a BF1101WR switch chip [16]. The control circuit can sequentially switch the reflection coefficient of each tag element.

2) *Radio receiver*: The radio receiver is implemented on a USRP N210. Signals are sampled at 4 MS/s and sent to a general purpose computer, where the designed algorithms are performed with National Instrument Labview software.

3) *COTS RFID system*: The COTS RFID reader Impinj R420 and ALN-9610 RFID tags that follow the EPC Gen2 protocol [17] and operate on 920 ~ 924 MHz are used [18], [19]. The reader is equipped with a 9dBi reader antenna.

V. PERFORMANCE EVALUATION

A. Methodology

1) *Setup*: The experiments are conducted in various indoor scenarios: a) room scenario; b) corridor scenario; c) NLOS scenario, as shown in Figure 16. In these scenarios, both the static case (the robot is static) and the mobile case (the robot is moving toward the object) are evaluated.

2) *Metric*: In the far range, the angular errors, defined as the differences between the true direction and the measured direction are collected. In the near range, the location errors, i.e., the differences between the true location and the measured location, are collected.

3) *Other approaches*: To the best of our knowledge, there is no existing RFID localization system based on portable tag array. Hence, the antenna array based localization systems are considered for comparison, which consists of single-channel based approaches [6], [10] and multi-channel based approaches [7], [20]. As our system operates on a single channel, the single-channel approaches [6], [10] are applied to the same system setup for comparison.

- **Arraytrack**: We compare POLO with Arraytrack [10] in the far range. In Arraytrack, the object's direction is estimated via a spatial smoothing based MUSIC algorithm.

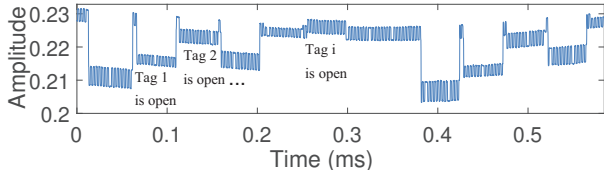


Fig. 17. The signals received by the receiver.

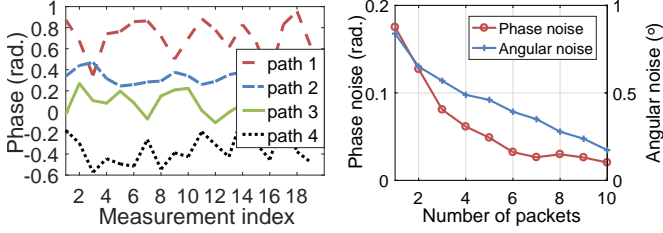


Fig. 18. The phase values of the estimated channel coefficients.

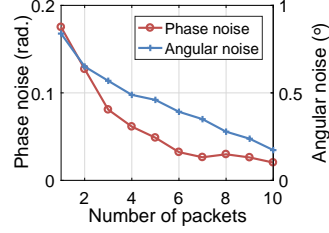


Fig. 19. The phase noise and the angular estimation noise.

- **RFLy**: We compare POLO with RFLy [6] in the near range. In RFLy, the object's 2D location is estimated via a location hologram.

B. Channel Estimation

The signals received by the receiver are shown in Figure 17. It can be observed that these signals are changed significantly when the reflection coefficient of a tag element is switched.

The phase values of the channel coefficients of the paths reflected by 4 tag elements of the tag array are shown in Figure 18, where the channel estimation is based on one packets. The variation of the results is due to the existing of noise. To reduce the noise, TCE is conducted based on multiple packets. The relation between the phase noise and the number of packets is shown in Figure 19. It is shown that when the number of packets exceeds eight, the phase noise is within 0.03 radian, and the angular noise in direction estimation is within 0.5 degree. Hence, to obtain a stable result, 8 packets are needed in TCE, which is acceptable, as a general commercial RFID reader can read 100 ~ 200 packets per second [21].

C. Direction Estimation

When the object is far from the mobile robot, SSDE is applied to estimate the object's direction.

1) *Effectiveness of the equivalent uniform array*: In SSDE, the equivalent uniform array is designed to solve the anisotropic coupling problem. The key parameter, equivalent element spacing $d_v(\theta)$ in Eq. (13), is measured and shown in Figure 20, where $\theta \in [-75^\circ, 75^\circ]$. It is shown that $d_v(\theta)$ varies with the object's direction θ , and the variation can exceed 0.6 cm, which denotes the influence of anisotropic coupling on the tag array is severe.

To validate effectiveness of the equivalent uniform array, the benchmark method Arraytrack in [10] is applied in portable locator (anisotropic coupling is not considered in the Arraytrack). The object is placed at the directions from -70° to 70° with a step of 2° . The distance between the

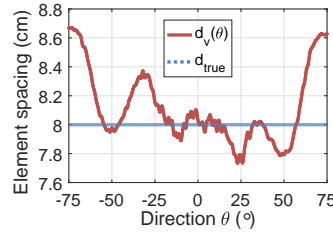


Fig. 20. The equivalent element spacing $d_v(\theta)$.

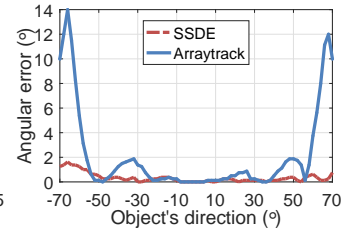


Fig. 21. The measurement results in $[-70^\circ, 70^\circ]$ range.

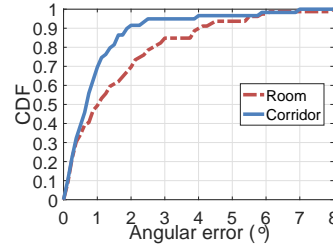


Fig. 22. The CDF of angular error in static case.

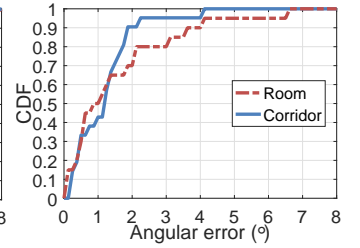


Fig. 23. The CDF of angular error in mobile case.

object and the portable locator is 6 m. The direction estimation errors of SSDE and Arraytrack are collected, as shown in Figure 21. It can be seen that Arraytrack is greatly affected by anisotropic coupling, and the estimation error exceeds 10° in some directions. In contrast, the SSDE scheme can resist anisotropic coupling, and achieves high accuracy of direction estimation in the range of $[-70^\circ, 70^\circ]$.

2) *Direction estimation in the static case*: SSDE is further evaluated in indoor scenarios: the room scenario and the corridor scenario shown in Figure 16. In the room scenario, the object is placed at 105 points individually. The distance between the object and the portable locator varies from 2 m to 6 m. Moreover, there exists much metal furniture in the room, which creates multipath reflections. In the corridor scenario, the object is placed at 50 points individually. The distance between the object and the portable locator varies from 2 m to 6 m. The walls in the corridor can generate strong NLOS reflections.

The cumulative distribution function (CDF) of the direction estimation error is shown in Figure 22. The average angular errors in the room scenario and the corridor scenario are 1.6° and 1.1° , respectively. The direction estimation accuracy in the room scenario is worse than that in the corridor case, as the room scenario has more severe multipath reflections than the corridor scenario.

3) *Direction estimation in the mobile case*: When the object's direction is measured, the robot can move towards the object. Hence, the direction estimation in the mobile case is evaluated. In the experiments, the robot measures the object's direction at multiple points on its way to the object. The CDF of the angular errors is shown in Figure 23. It can be observed that the angular error in the mobile case is close to that in the static case. Hence, direction estimation accuracy is not greatly influenced by the robot's mobility.

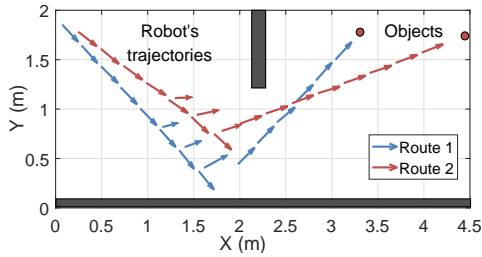


Fig. 24. Localization results in NLOS case.

4) *Direction estimation in the NLOS case:* When the LOS path between the object and the portable locator is blocked, the robot can follow the NLOS path to approach the object. The corresponding experiments are shown by the NLOS case in Figure 16. The direction estimation results are shown by the arrows in Figure 24. It can be observed that, at the first several points, the locator can only estimate the direction of the NLOS path. The robot moves towards the wall that reflects the NLOS path. When the LOS path between the object and the locator appears, the locator obtains two directions and decides which one is LOS path. As the direction of the LOS path is more stable than that of the NLOS path, the locator chooses the LOS path and approaches the object. Hence, POLO can locate the objects in the NLOS case.

D. Location Estimation

When the object is in the proximity of the portable locator, the object's 2D location can be estimated via NRP scheme.

1) *Effectiveness of the anisotropic coupling calibration:* In this experiment, the core algorithm in the RFLy [6] is applied in the same system for comparison. The anisotropic coupling is not considered in the RFLy. The object is placed at 80 points individually, and the distance between the object and the tag array varies from 0.4 m to 1 m. The localization errors in RFLy and NRP are shown in Figure 25. It can be seen that the mean of location error of NRP is within 5 cm in both the room scenario and the corridor scenario, and NRP reduces the location error by 50%.

In the near range, the multipath reflections from environment are not severe, as the object is in the locator's proximity. The localization accuracy is mainly influenced by anisotropic coupling, which is eliminated in NRP scheme.

VI. RELATED WORK

1) *Antenna array based localization systems:* In [22], [23], two or three antenna arrays are deployed in separate points as positioning anchors. Each antenna array can measure the object's direction individually. The object is located by the triangulation principle. In [24], a novel RFID tag array is deployed on an object to measure the object's orientation. Based on the object's orientation, the object's location is determined by two separate reader antennas. However, these systems are not feasible for mobile robots due to the use of multiple separate antenna arrays or separate antennas. In [1], [2], [4], several advanced positioning algorithms are developed

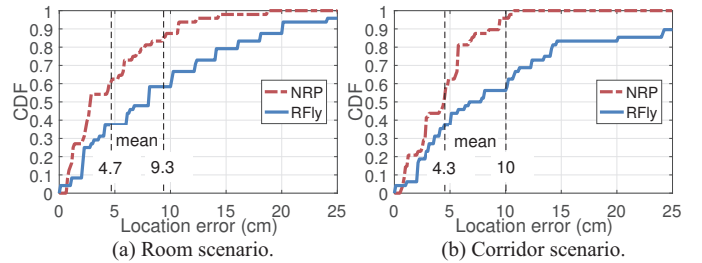


Fig. 25. The CDF of location error.

based on a linear antenna array that consists of 4 RFID reader antennas. In [3], a well-designed antenna array that consists of 8 RFID reader antennas is developed to measure the trajectory of an RFID tag. These schemes achieve excellent accuracy (6.5 ~ 12 cm). However, they are infeasible for mobile robots.

2) *Moving antenna based positioning systems:* In [5]–[7], the SAR technology is applied to emulate an antenna array via a moving RFID reader antenna with known locations. In [5], an RFID reader antenna is carried by a robot moving in a straight line (with known locations) to collect the multipath profiles of reference tags, and locate the objects in the reference tags' proximity. In [6], an RFID relay is carried by a drone. The location of the drone is measured by a camera based localization system. In [7], an RFID reader antenna is moving on a rail, and the location of the antenna is measured by a laser distance meter. In these localization schemes, a high accuracy of 5 ~ 12 cm can be achieved in the indoor environment. However, the high-accuracy tracking of moving RFID antennas restricts the mobility of the moving equipment, by requiring its movement on a linear guide [5] or a rail [7], or demanding support from an anchor [6]. Such restrictions make these schemes infeasible for mobile robots due to the need of roaming in the entire factory.

VII. CONCLUSION

In this paper, a portable localization system POLO has been developed for a mobile robot to locate an RFID-tagged object. In POLO, a foldable tag array is associated with a receiver, with which backscatter channels between the target object and each element of the tag array can be accurately estimated by eliminating the anisotropic coupling among tags. As a result, the direction to the target can be estimated when the robot is in the far range, and 2D location of the target can be determined when the robot approaches the target along the estimated direction. We have implemented a prototype system. POLO is lightweight and can accurately locate an RFID-tagged object in various indoor scenarios. In addition, an object in NLOS can also be pinpointed. POLO is currently designed to operate in single channel. Future study is needed to further improve its performance by considering multiple-channel operation.

VIII. ACKNOWLEDGMENT

This work was supported by National Natural Science Foundation of China (NSFC) under grant 61771312.

REFERENCES

- [1] T. Liu, L. Yang, Q. Lin, Y. Guo, and Y. Liu, "Anchor-free backscatter positioning for RFID tags with high accuracy," in *Proc. IEEE INFOCOM*, 2014, pp. 379–387.
- [2] L. Yang, Y. Chen, X.-Y. Li, C. Xiao, M. Li, and Y. Liu, "Tagoram: real-time tracking of mobile RFID tags to high precision using COTS devices," in *Proc. ACM MobiCom*, 2014, pp. 237–248.
- [3] J. Wang, D. Vasisht, and D. Katabi, "RF-IDraw: virtual touch screen in the air using RF signals," in *Proc. ACM SIGCOMM*, vol. 44, no. 4, 2014, pp. 235–246.
- [4] F. Xiao, Z. Wang, N. Ye, R. Wang, and X.-Y. Li, "One more tag enables fine-grained RFID localization and tracking," *IEEE/ACM Trans. Netw.*, vol. 26, no. 1, pp. 161–174, 2018.
- [5] J. Wang and D. Katabi, "Dude, where's my card?: RFID positioning that works with multipath and non-line of sight," in *Proc. ACM SIGCOMM*, vol. 43, no. 4, 2013, pp. 51–62.
- [6] Y. Ma, N. Selby, and F. Adib, "Drone relays for battery-free networks," in *Proc. ACM SIGCOMM*, 2017, pp. 335–347.
- [7] H. Xu, D. Wang, R. Zhao, and Q. Zhang, "FaHo: deep learning enhanced holographic localization for RFID tags," in *Proc. ACM SenSys*, 2019, pp. 351–363.
- [8] J. P. Fitch, *Synthetic aperture radar*. Springer Science & Business Media, 2012.
- [9] T.-J. Shan, M. Wax, and T. Kailath, "On spatial smoothing for direction-of-arrival estimation of coherent signals," *IEEE Trans. Acoustics, Speech, and Signal Proc.*, vol. 33, no. 4, pp. 806–811, 1985.
- [10] J. Xiong and K. Jamieson, "Arraytrack: a fine-grained indoor location system," in *Proc. USENIX NSDI*, 2013, pp. 71–84.
- [11] W. L. Stutzman and G. A. Thiele, *Antenna theory and design*. John Wiley & Sons, 2012.
- [12] D. Tse and P. Viswanath, *Fundamentals of wireless communication*. Cambridge university press, 2005.
- [13] H. T. Hui, M. E. Bialkowski, and H. S. Lui, *Mutual coupling in antenna arrays*. Hindawi, 2010.
- [14] R. Schmidt, "Multiple emitter location and signal parameter estimation," *IEEE Trans. Antennas Propag.*, vol. 34, no. 3, pp. 276–280, 1986.
- [15] Mixed signal microcontroller. [Online]. Available: <http://www.ti.com/lit/ds/symlink/msp430g2553.pdf>
- [16] BF1101WR N-channel dual-gate MOS-FETs. [Online]. Available: https://www.nxp.com/docs/en/data-sheet/BF1101R_W_R.pdf
- [17] D. M. Dobkin, *The RF in RFID: UHF RFID in practice*. Newnes, 2012.
- [18] Impinj, Speedway Revolution Reader Application Note, "Low level user data support," *Impinj, Seattle, Wash, USA*, 2013.
- [19] ALN-9610 squiggle inlay. [Online]. Available: [http://www.alientechnology.com/wp-content/uploads/ALN-9610%20Squig%20Higgs3%20\(2015-12-18\).pdf](http://www.alientechnology.com/wp-content/uploads/ALN-9610%20Squig%20Higgs3%20(2015-12-18).pdf)
- [20] L. Shangguan and K. Jamieson, "The design and implementation of a mobile RFID tag sorting robot," in *Proc. ACM MobiSys*, 2016, pp. 31–42.
- [21] K. M. Ramakrishnan and D. D. Deavours, "Performance benchmarks for passive UHF RFID tags," in *Proc. 13th GIITG Conf. Meas., Model. Eval. Comput. Commun. Syst.*, 2006, pp. 1–18.
- [22] C. Hekimian-Williams, B. Grant, X. Liu, Z. Zhang, and P. Kumar, "Accurate localization of RFID tags using phase difference," in *IEEE RFID*, 2010, pp. 89–96.
- [23] M. Cremer, U. Dettmar, C. Hudusch, R. Kronberger, R. Lerche, and A. Pervez, "Localization of passive UHF RFID tags using the aoact transmitter beamforming technique," *IEEE Sens. J.*, vol. 16, no. 6, pp. 1762–1771, 2015.
- [24] D. Xie, D. Weidman, S. Yao, A. Tang, and X. Wang, "3D passive positioning based on RFID tag array," in *Proc. IEEE ICC*, 2019, pp. 1–6.